PNAS RESEARCH ARTICLE | CELL BIOLOGY OPEN ACCESS

Hepatic SEL1L-HRD1 ER-associated degradation regulates systemic iron homeostasis via ceruloplasmin

Pattaraporn Thepsuwan[a], Asmita Bhattacharya[b], Zhenfeng Song[a], Stephen Hippleheuser[a], Shaobin Feng[a], Xiaoqiong Wei[b], Nupur K. Das[b], Mariana Sierra[c], Juncheng Wei[d], Deyu Fang[d], Yu-ming M. Huang[c], Kezhong Zhang[a,e], Yatrik M. Shah[b,f], and Shengyi Sun[a,e,1]

Edited by Miguel P. Soares, Instituto Gulbenkian de Ciencia, Oeiras, Portugal; received July 22, 2022; accepted November 18, 2022 by Editorial Board Member Brenda A. Schulman

Iron homeostasis is critical for cellular and organismal function and is tightly regulated to prevent toxicity or anemia due to iron excess or deficiency, respectively. However, subcellular regulatory mechanisms of iron remain largely unexplored. Here, we report that SEL1L-HRD1 protein complex of endoplasmic reticulum (ER)-associated degradation (ERAD) in hepatocytes controls systemic iron homeostasis in a ceruloplasmin (CP)-dependent, and ER stress-independent, manner. Mice with hepatocyte-specific *Sel1L* deficiency exhibit altered basal iron homeostasis and are sensitized to iron deficiency while resistant to iron overload. Proteomics screening for a factor linking ERAD deficiency to altered iron homeostasis identifies CP, a key ferroxidase involved in systemic iron distribution by catalyzing iron oxidation and efflux from tissues. Indeed, CP is highly unstable and a bona fide substrate of SEL1L-HRD1 ERAD. In the absence of ERAD, CP protein accumulates in the ER and is shunted to refolding, leading to elevated secretion. Providing clinical relevance of these findings, SEL1L-HRD1 ERAD is responsible for the degradation of a subset of disease-causing CP mutants, thereby attenuating their pathogenicity. Together, this study uncovers the role of SEL1L-HRD1 ERAD in systemic iron homeostasis and provides insights into protein misfolding-associated proteotoxicity.

SEL1L-HRD1 ERAD | ceruloplasmin | iron metabolism | hepatocytes

Significance

Systemic iron metabolism is key for cellular and organismal function. However, the subcellular regulatory mechanisms of iron homeostasis remain poorly understood. This study highlights the pathophysiological significance of a principal cellular protein quality-control mechanism known as endoplasmic reticulum-associated degradation (ERAD) in systemic iron homeostasis, in part by regulating the abundance of ceruloplasmin, a key ferroxidase. Hence, this study uncovers a previously unappreciated regulatory mechanism in iron metabolism as well as a function for ERAD.

Systemic iron metabolism is tightly regulated for cellular and organismal function. Iron is stored in the hepatocytes and distributed to the peripheral tissues through an intricate process: Ferrous iron (Fe^{2+}) is exported from hepatocytes via the iron exporter ferroportin (FPN1) and subsequently oxidized at the plasma membrane by a ferroxidase known as ceruloplasmin (CP) to ferric iron (Fe^{3+}) prior to be loaded onto transferrin (TF) in the circulation (1–4). Iron-loaded TF can then be endocytosed by cells via TF receptor 1 (TFR1), while TF receptor 2 (TFR2) on hepatocytes senses blood iron levels to modulate the expression of a key iron-regulating hormone, hepcidin (2, 3). Gain- or loss-of-function of any of the aforementioned factors such as FPN1, CP, TF, hepcidin, and TFR1/2 alters systemic iron metabolism, leading to either toxicity or anemia due to iron excess or deficiency, respectively, in mice and humans (2, 5–7). However, while most of these factors are synthesized in the endoplasmic reticulum (ER) as either membrane or secreted proteins, molecular details underlying their biogenesis in the ER remained largely unexplored.

ER-associated degradation (ERAD) is a principal ER quality-control mechanism that targets misfolded ER proteins for cytosolic proteasomal degradation (8, 9). The SEL1L-HRD1 protein complex represents the most evolutionarily conserved ERAD (10–17). Using conditional and cell type-specific *Sel1L*-deficient mice, we showed that SEL1L is an obligatory cofactor for the E3 ligase HRD1 (18). Subsequent studies from several laboratories have collectively demonstrated a critical physiological and pathological importance of this ERAD complex in various cell types in energy metabolism, food intake, immunity, gut and kidney homeostasis, cartilage development, and quiescence of hematopoietic stem cells (19–33). However, the significance of SEL1L-HRD1 ERAD in iron metabolism remains unknown.

In this study, we report the role of hepatocyte-specific SEL1L-HRD1 ERAD in systemic iron homeostasis by regulating the maturation and turnover of CP in the ER. Mice with hepatocyte-specific *Sel1L* deficiency have altered basal iron homeostasis and altered response to iron deficiency and overload. Mechanistically, SEL1L-HRD1 ERAD mediates the proteasomal degradation of both endogenous and disease mutants of CP proteins, thereby regulating its abundance in the circulation and limiting their pathogenicity, respectively.

Author contributions: S.S. designed research; P.T., A.B., Z.S., S.H., S.F., X.W., M.S., Y.-m.M.H., and S.S. performed research and analyzed data; N.K.D., J.W., D.F., K.Z., and Y.M.S. contributed new reagents/analytic tools; and S.S. wrote the paper.

The authors declare no competing interest.

This article is a PNAS Direct Submission. M.P.S. is a guest editor invited by the Editorial Board.

[1]To whom correspondence may be addressed. Email: shengyisun@wayne.edu.

This article contains supporting information online at https://www.pnas.org/lookup/suppl/doi:10.1073/pnas.2212644120/-/DCSupplemental.

Published January 3, 2023.

Results

***Sel1L^{AlbCre}* Mice Have Altered Iron Homeostasis under Basal Condition.** Iron overload induced by a 2-wk feeding of a high iron diet (HID, containing 800 or 8,800 ppm iron) elevated the expression of ER chaperone *BiP* and *Sel1L-Hrd1* ERAD by 2 to 5 folds in a dose-dependent manner (Fig. 1*A*). Intraperitoneal injection of iron dextran (Fe-dex) induced similar changes in ERAD and *BiP* expression (Fig. 1*B*). On the other hand, iron deficiency following a 3-wk feeding of an iron-deficient diet (IDD, containing <5 ppm iron) failed to affect ERAD and *BiP* expression (Fig. 1*C*). As expected, *Hepc* gene (encoding hepcidin) in the liver was up- or down-regulated in iron overload or deficient models (Fig. 1 *A*–*C*).

We next explored the importance of hepatic SEL1L-HRD1 ERAD in iron metabolism using our previously generated hepatocyte-specific *Sel1L*-deficient (*Sel1L$^{flox/flox}$;Albumin-Cre*, *Sel1L^{AlbCre}*) mice (27). On a regular chow diet containing 240 ppm (240 mg/kg) iron, male *Sel1L^{AlbCre}* mice exhibited a transient growth retardation at 6 to 9 wk of age as shown previously (27), and appeared largely normal after 10 wk of age compared with wild-type (WT) (*Sel1L$^{flox/flox}$*, *WT*) littermates (Fig. 1*D*). Measurement of tissue iron distribution revealed an altered distribution of non-heme iron in 10-wk-old *Sel1L^{AlbCre}* mice: reduced iron contents by over 30% in the liver, while elevated by 15% in the heart of *Sel1L^{AlbCre}* mice compared with *WT* littermates (Fig. 1*E*). By contrast, iron contents in other tissues (e.g. spleen, pancreas, kidney, duodenum and feces) were comparable between the cohorts (Fig. 1*E* and *SI Appendix*, Fig. S1*A*), so were the circulating levels of iron and ferritin (Fig. 1*F* and *SI Appendix*, Fig. S1*B*). Similar findings were obtained in the female cohorts fed with a regular chow diet or an iron-sufficient control diet containing 35 ppm iron (Fig. 1 *G*–*I* and *SI Appendix*, Fig. S1 *C*–*E*): while growth retardation was normalized by 14 wk of age (Fig. 1*G*), iron contents in both the liver and spleen were reduced by 40% in 14-wk-old female *Sel1L^{AlbCre}* mice (Fig. 1*H* and *SI Appendix*, Fig. S1*E*). Complete blood count (CBC) parameters were not affected by the loss of *Sel1L* (*SI Appendix*, Fig. S1*F*). Moreover, in both genders, hepatic contents of another essential micromineral, copper, were not affected by the loss of *Sel1L* (*SI Appendix*, Fig. S1*G*), uncoupling reduced hepatic iron levels from possible copper deficiency. In keeping with the role of SEL1L in SEL1L-HRD1 ERAD, hepatic iron content was also reduced in hepatocyte-specific *Hrd1*-deficient (*Hrd1$^{flox/flox}$;Albumin-Cre*, *Hrd1^{AlbCre}*) mice (28) (Fig. 1*J*). Taken together, these results suggest that hepatic SEL1L-HRD1 ERAD may be involved in hepatic and systemic iron metabolism under basal condition.

***Sel1L^{AlbCre}* Mice Are Hypersensitive to Iron Deficiency-Induced Anemia.** We next explored the pathological significance of hepatocyte SEL1L-HRD1 ERAD in iron deficiency following a 4-wk feeding of IDD. Both *WT* and *Sel1L^{AlbCre}* mice grew normally under iron deficiency (Fig. 2*A*). IDD feeding progressively depleted hepatic and splenic iron contents to nearly undetectable levels (Fig. 2*B*) and induced anemia in both *WT* and *Sel1L^{AlbCre}* mice as evidenced by significant reductions in hemoglobin (HB), hematocrit (HCT), mean corpuscular volume (MCV), and mean corpuscular hemoglobin, along with elevated numbers of red blood cells and red cell distribution width (Fig. 2*C* and *SI Appendix*, Fig. S2*A*). However, in comparison with *WT* littermates, the response to IDD was more pronounced and rapid in *Sel1L^{AlbCre}* mice (Fig. 2 *B* and *C*). As a control, iron deficiency had no effect on other cell types such as blood platelets, eosinophils, or basophils (*SI Appendix*, Fig. S2*B*). Taken together, these data suggest that hepatic SEL1L deficiency predisposes mice to iron deficiency-induced anemia.

***Sel1L^{AlbCre}* Mice Are Resistant to Hepatic Iron Overload.** We next explored the importance of ERAD under iron overload using the following two experimental models. We first placed female *Sel1L^{AlbCre}* and *WT* littermates on HID containing 800 ppm iron for a total of 8 wk. Both cohorts grew comparably under HID feeding and had similar daily food intake (Fig. 2*D* and *SI Appendix*, Fig. S2*C*). HID dramatically increased hepatic and splenic iron contents in *WT* mice, but to a much lesser extent

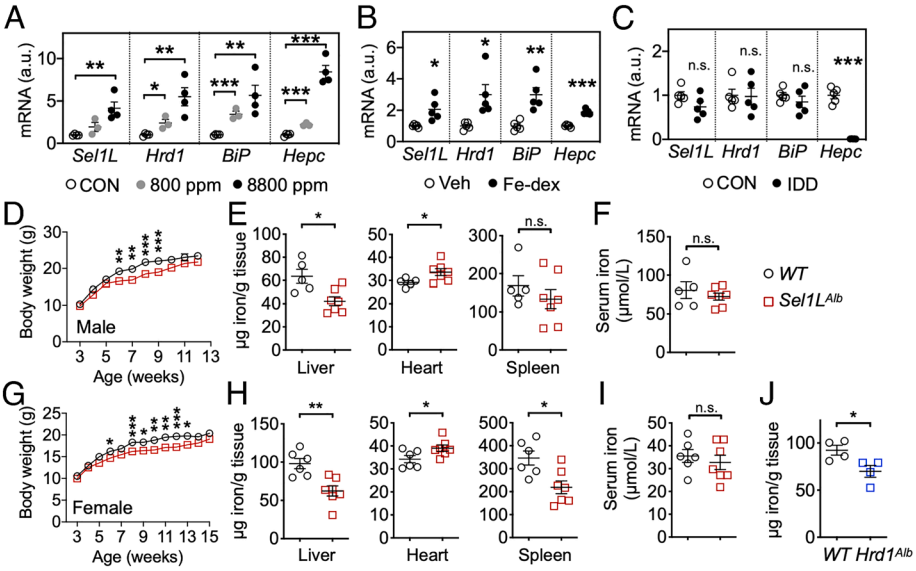

Fig. 1. Hepatocyte-specific *Sel1L* deficiency leads to altered iron homeostasis under basal condition. (*A*–*C*) qPCR analyses in livers from (*A*) 7-wk-old WT mice 2 wk post a control (CON, 35 ppm iron) or HID (800 or 8,800 ppm iron) feeding, n = 3 to 4; (*B*) 8-wk-old WT mice 3 d post an intraperitoneal injection of vehicle (Veh) or iron-dextran (Fe-dex) at 20 mg/kg body weight, n = 5; (*C*) 7-wk-old WT mice 3 wk post a control (35 ppm iron) or IDD (<5 ppm iron) feeding, n = 5. (*D*–*I*) Growth curve (*D*, *G*), non-heme iron contents in tissues (*E*, *H*) and blood serum (*F*, *I*) of 10-wk-old male (*D*–*F*) and 14-wk-old female (*G*–*I*) *WT* and *Sel1L^{AlbCre}* littermates fed with a chow diet. N ≥ 8 for growth curve, and n = 5 to 7 for iron measurements. (*J*) Non-heme iron content in the livers of 12-wk-old male *WT* and *Hrd1^{AlbCre}* littermates fed with a chow diet. N = 4. Values, mean ± SEM. **P* < 0.05; ***P* < 0.01; ****P* < 0.001; n.s., not significant by Student's *t* test for two-group comparisons, or two-way ANOVA with the Tukey multiple comparison test in *D* and *G*.

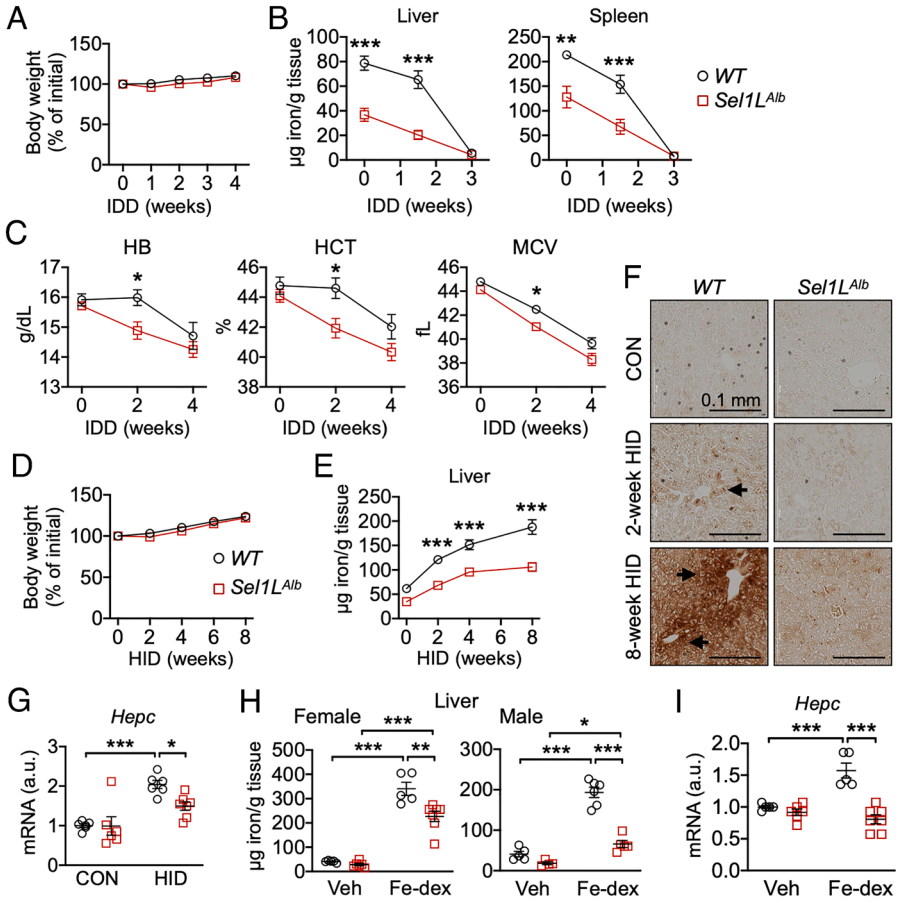

Fig. 2. *Sel1L*^{AlbCre} mice exhibit altered response to iron deficiency as well as iron overload. (*A*–*C*) 7-wk-old *WT* and *Sel1L*^{AlbCre} female littermates were treated with control (35 ppm iron) or IDD (<5 ppm iron) for up to 4 wk. Changes in body weight as a percentage of initial weight (*A*), non-heme iron contents in tissues (*B*), and CBC (*C*) are shown. HB, hemoglobin; HCT, hematocrit; MCV, mean corpuscular volume. N = 14 for body weight and CBC, n = 5 to 9 for tissue iron content. (*D*–*G*) 7-wk-old *WT* and *Sel1L*^{AlbCre} female littermates were treated with control (35 ppm iron) or HID (800 ppm iron) for up to 8 wk. Changes in body weight as a percentage of initial weight (*D*), non-heme iron content in livers (*E*), DAB-enhanced Prussian blue staining of livers (*F*), and qPCR analysis of livers after 2-wk HID feeding (*G*) are shown. In *F*, arrows point to the periportal deposition of iron stained in brown. N = 9 to 14 for body weight and liver iron content, n = 3 to 4 for tissue staining, and n = 6 to 7 for qPCR. (*H* and *I*) 8-wk-old female or male *WT* and *Sel1L*^{AlbCre} littermates were intraperitoneally injected with vehicle (Veh) or iron-dextran (Fe-dex) at 20 mg/kg body weight. 3 d later, non-heme iron content in livers were measured (*H*). qPCR analysis of livers from female littermates are shown in (*I*). Females, n = 5 to 7; males, n = 4 to 6. Values, mean ± SEM. **P* < 0.05; ***P* < 0.01; ****P* < 0.001 by two-way ANOVA with the Tukey multiple comparison test.

in *Sel1L*^{AlbCre} mice (Fig. 2 *E* and *F* and *SI Appendix*, Fig. S2*D*). In contrast, iron levels in the other tissues such as the kidney and serum were comparable between the cohorts, while mildly elevated in the heart of *Sel1L*^{AlbCre} mice (*SI Appendix*, Fig. S2*D*). Similar observation of increased resistance to iron overload was made in male *Sel1L*^{AlbCre} mice (*SI Appendix*, Fig. S2*E*). In keeping with these findings, hepatic expression of *Hepc* was significantly elevated in *WT* mice, but not in *Sel1L*^{AlbCre} mice, following weeks of HID feeding (Fig. 2*G*).

To exclude possible contributions from food intake and/or enteric iron absorption, we next performed a direct intraperitoneal injection of iron dextran (Fe-dex) (34, 35), which led to iron overload in the livers of both male and female *WT* mice (Fig. 2*H*). Iron accumulation mainly occurred in macrophages in the liver (arrowheads, *SI Appendix*, Fig. S2F) (36). In contrast, hepatic iron content was significantly lower in *Sel1L*^{AlbCre} mice compared with *WT* littermates (Fig. 2*H* and *SI Appendix*, Fig. S2*F*). Similar to the HID model, the induction of *Hepc* expression was abolished in *Sel1L*^{AlbCre} mice compared with that in *WT* mice (Fig. 2*I*). Taken together, our results indicate that hepatic SEL1L-HRD1 ERAD regulates hepatic iron content and partitioning under both basal and pathological conditions of iron deficiency and overload.

Identification of CP, but Not ER stress, As a Possible Link Between ERAD and Iron Metabolism. The forementioned data pointed to either a reduced iron deposition or accelerated iron export from the liver in the absence of SEL1L-HRD1 ERAD. We next explored how ERAD controls iron metabolism in the liver. Given our previous report of increased cAMP-responsive element-binding protein H (CREBH) activity and expression of fibroblast growth factor 21 (FGF21) in *Sel1L*^{AlbCre} mice (27), and given the reported role of CREBH in iron metabolism (37), we first tested whether elevated CREBH and FGF21 expression affects iron deposition. Interestingly, unlike those in *Sel1L*^{AlbCre} mice, iron contents were elevated in the livers of mice overexpressing active CREBH (Fig. 3*A* and *SI Appendix*, Fig. S3*A*) or FGF21 (Fig. 3*B* and *SI Appendix*, Fig. S3*B*), hence excluding a major role of CREBH-FGF21 in altered iron metabolism in *Sel1L*^{AlbCre} mice.

We next determined the role of unfolded protein response (UPR) in iron homeostasis, as we previously showed that *Sel1L* deficiency triggers a very mild UPR in the liver (27). We tested two pharmacological ER stress inducers, tunicamycin that inhibits ER protein glycosylation (38), and cyclopiazonic acid (CPA) that depletes ER calcium (39). While tunicamycin induced a strong UPR (*SI Appendix*, Fig. S3 *C* and *D*), CPA induced a mild UPR, comparable to the level observed in *Sel1L*^{AlbCre} livers (*SI Appendix*,

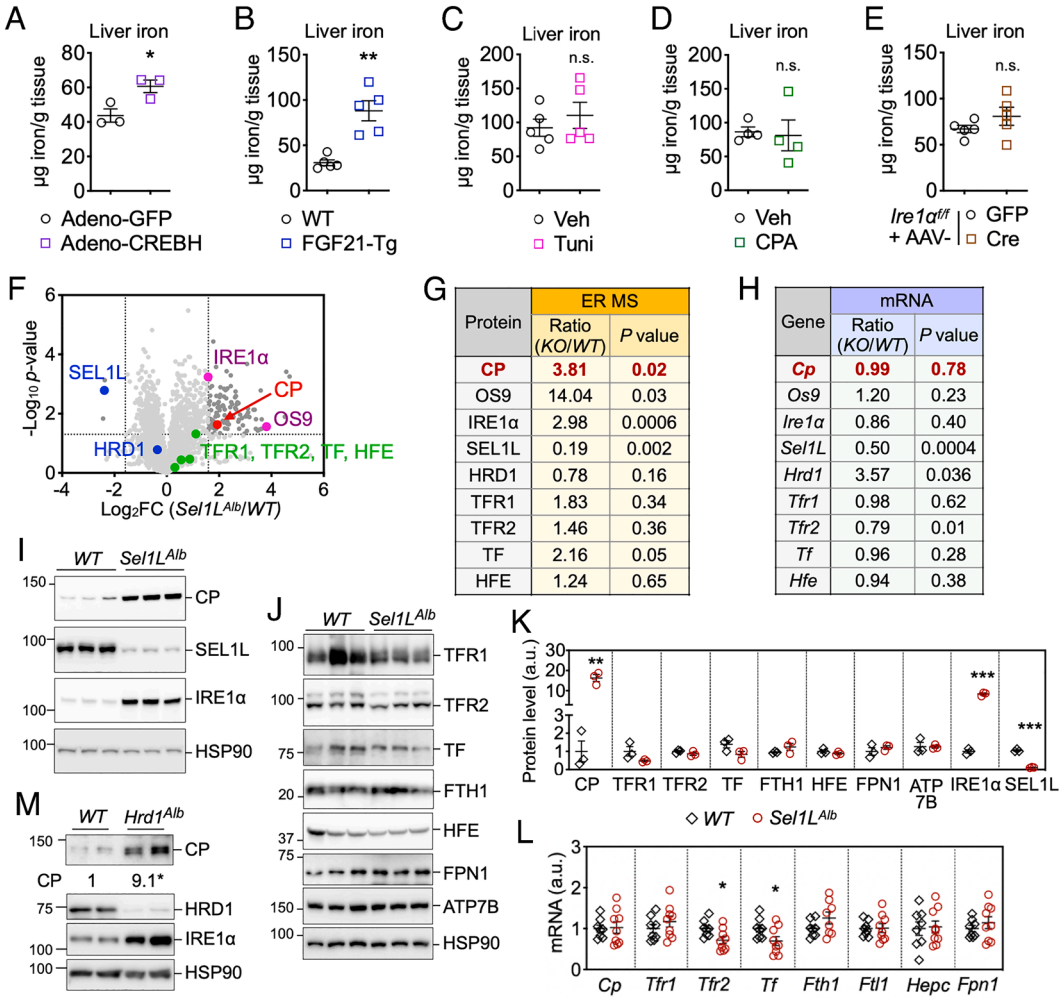

Protein	ER MS	
	Ratio (*KO*/*WT*)	*P* value
CP	**3.81**	**0.02**
OS9	14.04	0.03
IRE1α	2.98	0.0006
SEL1L	0.19	0.002
HRD1	0.78	0.16
TFR1	1.83	0.34
TFR2	1.46	0.36
TF	2.16	0.05
HFE	1.24	0.65

Gene	mRNA	
	Ratio (*KO*/*WT*)	*P* value
Cp	**0.99**	**0.78**
Os9	1.20	0.23
Ire1α	0.86	0.40
Sel1L	0.50	0.0004
Hrd1	3.57	0.036
Tfr1	0.98	0.62
Tfr2	0.79	0.01
Tf	0.96	0.28
Hfe	0.94	0.38

Fig. 3. CP, but not ER stress, is a possible link between SEL1L-HRD1 ERAD and iron metabolism. (*A–E*) Hepatic iron content in (*A*) *WT* mice 5 d after an intravenous injection of adenovirus overexpressing CREBH or GFP; (*B*) 4-mo-old hepatocyte-specific ApoE promoter-driven FGF21 transgenic or *WT* littermates; (*C*) *WT* mice 4 h after an intraperitoneal injection of tunicamycin (Tuni) at 0.1 mg/kg body weight; (*D*) *WT* mice 4 h after an intraperitoneal injection of CPA at 10 mg/kg body weight; (*E*) *Ire1α*$^{f/f}$ mice 3 wk after an intravenous injection of AAV8-expressing hepatocyte-specific TBG promoter-driven Cre or GFP. N = 3 to 5. (*F* and *G*) Volcano plot (*F*) and table (*G*) of proteomics analysis of purified microsomes from *WT* and *Sel1L*^{AlbCre} (*KO*) livers. In (*F*), X- and Y-axes correspond to log2 fold change and -log10 *P*-value, respectively. The horizontal and vertical dotted lines represent *P*-value of 0.05 and fold change of 3, respectively. (*H*) Microarray analysis showing transcript levels of the same set of genes as (*G*) in *WT* and *Sel1L*^{AlbCre} (KO) livers. (*I–K*) Western blot analysis in 10-wk-old female *WT* and *Sel1L*^{AlbCre} livers, with quantitation normalized to HSP90 shown in (*K*). N = 3 each group. (*L*) qPCR analysis in *WT* and *Sel1L*^{AlbCre} livers. *WT*, n = 8; *Sel1L*^{AlbCre}, n = 9. (*M*) Western blot analysis in 12-wk-old male *WT* and *Hrd1*^{AlbCre} livers, with quantitation of CP normalized to HSP90 shown below the blot. Values, mean ± SEM. **P* < 0.05; ***P* < 0.01; ****P* < 0.001; n.s. or not labeled, not significant by Student's *t* test.

Fig. S3 *C* and *E*). Neither CPA or tunicamycin, however, was able to alter hepatic iron content (Fig. 3 *C* and *D*). Moreover, the acute deletion of a key UPR sensor inositol-requiring enzyme-1α (IRE1α) in the hepatocytes did not alter hepatic iron content in mice fed on a chow diet (Fig. 3*E* and *SI Appendix*, Fig. S3*F*). Together, these data exclude possible roles of elevated CREBH, FGF21, or UPR in altered iron homeostasis in *Sel1L*^{AlbCre} mice.

A nonbiased microsomal proteomics screen (40) coupled with transcriptomics analysis (GSE118658) were performed in the laboratory to identify endogenous protein substrates regulated by SEL1L-HRD1 ERAD in hepatocytes. A total of 115 and 3 proteins were significantly up- or down-regulated by over threefolds, respectively, in the ER of *Sel1L*^{AlbCre} livers relative to that of *WT* livers (Fig. 3*F* and Dataset S1) (40). Expectedly, both SEL1L and HRD1 proteins were reduced, while two known ERAD substrates, UPR sensor IRE1α and ER lectin OS9 (29, 41), were significantly overrepresented in the *Sel1L*^{AlbCre} livers compared with *WT* livers (Fig. 3 *F* and *G*), thereby validating the analysis. Excitingly, we found that the CP protein was significantly elevated by ~3.8 fold in the ER of *Sel1L*^{AlbCre} livers (Fig. 3 *F* and *G*). By contrast, other iron regulatory proteins such as TFR1, TFR2, TF, and hereditary hemochromatosis protein (HFE) were either unchanged or moderately elevated (Fig. 3 *F* and *G*). Transcriptomic profiling showed that the *Cp* mRNA level was unchanged between the two cohorts (Fig. 3*H*) (27). These findings were confirmed by western blot, enzyme-linked immunosorbent assay (ELISA), and qPCR analyses: CP protein level was elevated by 16 fold in the livers of *Sel1L*^{AlbCre} mice, while other iron factors such as TFR1/2, TF, ferritin, HFE, FPN1, a copper transporter ATP7B, as well as serum hepcidin were unchanged (Fig. 3 *I* and *J*, quantitated in Fig. 3*K* and *SI Appendix*, Fig. S3*G*). Transcriptionally, *Cp*, as well as most of other iron factors, were unchanged in *Sel1L*^{AlbCre} livers, suggesting a posttranscriptional regulation of CP (Fig. 3*L*). In addition, the CP protein was markedly elevated in *Sel1L*^{AlbCre} livers not only under basal condition, but also under both HID and IDD conditions (*SI Appendix*, Fig. S3 *H* and *I*). Further establishing the link between SEL1L-HRD1 ERAD and CP, similar extent of CP accumulation was observed in the livers of *Hrd1*^{AlbCre} mice (Fig. 3*M*).

Together, these data demonstrate that CP is accumulated in the livers with impaired SEL1L-HRD1 ERAD function.

CP Is a Bona Fide Endogenous SEL1L-HRD1 ERAD Substrate. We next determined the molecular link between CP and SEL1L-HRD1 ERAD. A previous study showed that CP is degraded by proteasomes in vitro (42); however, the molecular details underlying this degradation event remained vague. Indeed, the endogenous CP protein was unstable with a half-life of about 4 h in *WT* primary hepatocytes, but became stabilized in the absence of SEL1L (Fig. 4*A*). The stability of CP was not affected by cellular iron levels, either with iron overload induced by ferric ammonium citrate (FAC) or iron depletion induced by deferoxamine (DFO) (*SI Appendix*, Fig. S3*J*). In vitro, the transfected CP-HA protein pulled down significantly more endogenous SEL1L and OS9 in *HRD1*$^{-/-}$ HEK293T cells than those in *WT* HEK293T cells (Fig. 4*B*). SEL1L-HRD1 ERAD were indeed indispensable for the polyubiquitination of CP-HA (Fig. 4 *C* and *D*) and HRD1 overexpression greatly enhanced CP polyubiquitination in an HRD1-ligase-dependent manner as demonstrated by the use of HRD1 ligase-dead mutant C2A variant (29) (Fig. 4*E*). Together, these data suggest that endogenous CP is highly misfolding prone in the ER and targeted for proteasomal degradation by SEL1L-HRD1 ERAD.

Enhanced Folding and Secretion of CP in the Absence of SEL1L-HRD1 ERAD. We next asked the significance of SEL1L-HRD1 ERAD on the maturation and folding of CP. CP, a secreted glycoprotein, is synthesized and folded in the ER of hepatocytes as an apoprotein with 6 N-glycosylation sites and, upon reaching the trans-Golgi network, is incorporated with its prosthetic group (copper ions) to become an active holoprotein (43–45). It is then distributed either in the liver or peripheral tissues such as the spleen to mediate the oxidation reaction of Fe^{2+} to Fe^{3+} thus iron export (4, 46). We first examined how ERAD affects CP protein maturation and secretion. To this end, we performed the endoglycosidase H (EndoH) digestion assay to distinguish CP pools that are in the ER with high mannose glycosylation (EndoH sensitive) vs. those that have matured and exited the ER with complex glycosylation (EndoH resistant). Unlike in *WT* livers where the majority of CP protein (83%) was EndoH resistant (Fig. 5*A*), the percentage of EndoH-resistant CP in the *Sel1L*^{AlbCre} livers reduced to 31% (Fig. 5*A*). However, as the total CP protein level was elevated in the *Sel1L*^{AlbCre} livers, the absolute amount of EndoH-resistant CP was increased in *Sel1L*^{AlbCre} livers compared with that of *WT* livers (Fig. 5*A*). In keeping with these findings, we observed significant increases of CP protein in both ER and non-ER fractions of *Sel1L*^{AlbCre} livers compared to those of *WT* livers (lanes 6 vs. 5 and 4 vs. 3, Fig. 5*B*). Moreover, splenic CP protein (derived from the liver) was doubled in *Sel1L*^{AlbCre}mice compared with that of *WT* mice (Fig. 5*C*), providing plausible explanation for the reduced splenic iron content in *Sel1L*^{AlbCre} mice (Figs. 1*H* and 2*B* and *SI Appendix*, Fig. S2*D*). Of note, the spleen does not express its own *Cp* gene (*SI Appendix*, Fig. S4*A*). These data demonstrate that SEL1L-HRD1 ERAD limits the amount of mature CP in the system by mediating its degradation.

The above finding of elevated CP secretion prompted us to test the hypothesis that misfolded CP protein in the ER of ERAD-deficient cells gains folding competency and thereby its function by undergoing additional folding. Indeed, CP protein in *Sel1L*^{AlbCre} livers interacted strongly with a major ER chaperone BiP, while the interaction was undetectable in *WT* livers (Fig. 5*D*). This points to a prolonged effort to fold "misfolded" CP in the absence of ERAD or alternatively (although less likely) target CP for degradation via other mechanism(s). Providing further support for the elevated secretion of functional CP, CP ferroxidase activity was

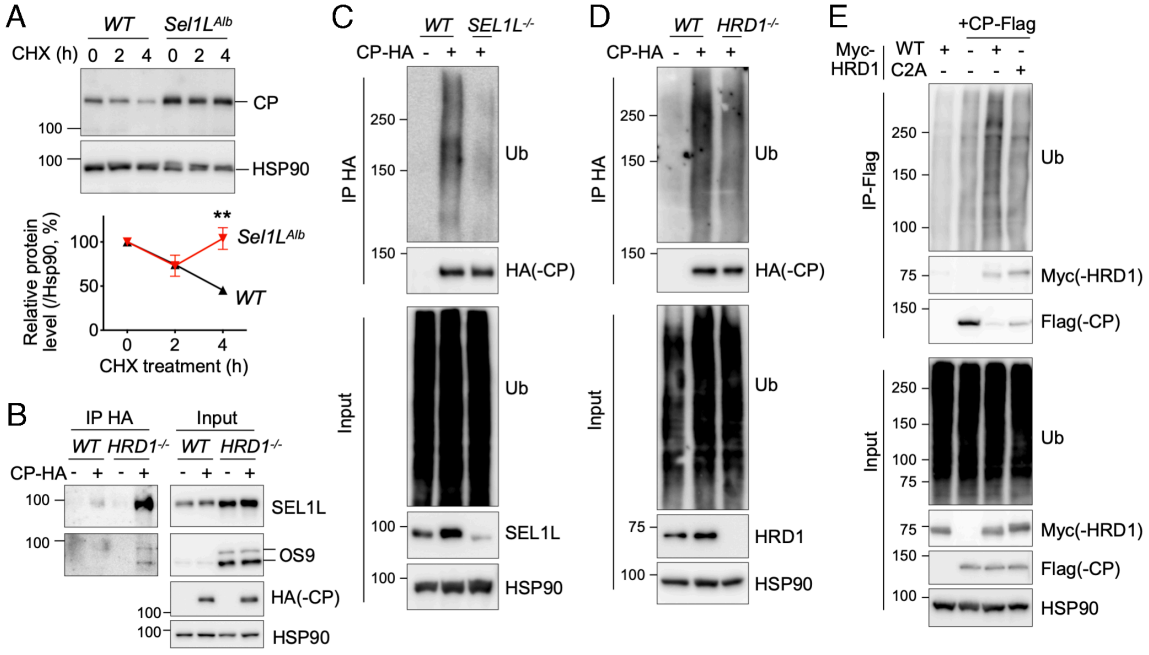

Fig. 4. Wildtype CP is degraded by SEL1L-HRD1 ERAD. (*A*) Western blot analysis of CP protein decay in primary hepatocytes treated with a translation inhibitor CHX. The degradation of CP is quantitated relative to the percentage of control. Values, mean ± SEM. $^{**}P < 0.01$ by two-way ANOVA with the Tukey multiple comparison test. (*B*) Western blot analysis of immunoprecipitates of HA-agarose in *WT* and HRD1-deficient (*HRD1*$^{-/-}$) HEK293T cells transfected with CP-HA, showing the interaction between CP, SEL1L and OS9. (*C* and *D*) Western blot analysis of immunoprecipitates of HA-agarose in *WT* and SEL1*L*$^{-/-}$ or *HRD1*$^{-/-}$ HEK293T cells transfected with CP-HA, showing that SEL1L and HRD1 are required for the ubiquitination of CP. (*E*) Western blot analysis of immunoprecipitates of Flag-agarose in *WT* HEK293T cells transfected with indicated plasmids, showing that HRD1 is sufficient for the ubiquitination of CP. HRD1 C2A, E3 ligase dead mutant. (*C*–*E*) Cells were treated with proteasome inhibitor MG132 for the last 3 h prior to immunoprecipitation. (*A*–*E*) Representative data from two independent experiments are shown.

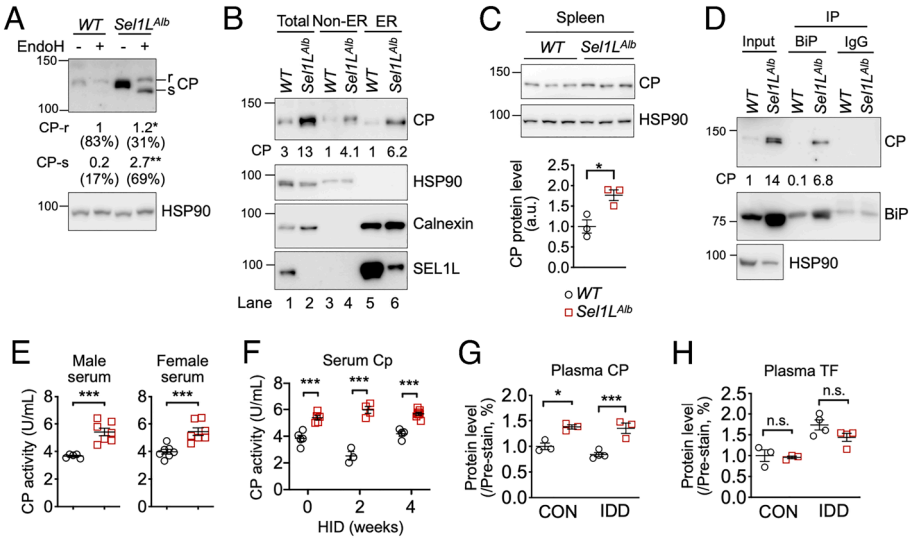

Fig. 5. SEL1L-HRD1 ERAD deficiency causes enhanced folding and secretion of CP. (*A*) Western blot analysis of CP in *WT* and *Sel1L*^{AlbCre} liver lysates treated with EndoH. Quantitation of absolute protein levels and percentages of EndoH-resistant (CP-r) and -sensitive (CP-s) CP from three independent repeats are shown. (*B*) Western blot analysis of CP in the ER and non-ER fractions of *WT* and *Sel1L*^{AlbCre} livers with quantitation of CP shown below. HSP90 and Calnexin, cytosolic and ER markers. Representative data from two independent repeats. (*C*) Western blot analysis of spleens from *WT* and *Sel1L*^{AlbCre} mice, with quantitation normalized to HSP90 shown below. (*D*) Western blot analysis of immunoprecipitates of ER chaperone BiP in *WT* and *Sel1L*^{AlbCre} liver lysates, showing the interaction between CP and BiP. Mouse IgG, a negative control. Quantitation of CP is shown below the blot. Representative data from two independent repeats. (*E*) Serum CP ferroxidase activity in 10-wk-old male and 14-wk-old female *WT* and *Sel1L*^{AlbCre} littermates. *WT*, n = 5 or 7; *Sel1L*^{AlbCre}, n = 7. (*F*) Serum CP ferroxidase activity in *WT* and *Sel1L*^{AlbCre} mice fed with control (CON, 35 ppm iron) or HID (800 ppm iron) for up to 4 wk. N = 3 to 8. (*G* and *H*) Quantitation of western blot analysis of plasma CP and TF proteins from *WT* and *Sel1L*^{AlbCre} mice after a control (CON, 35 ppm iron) or IDD (<5 ppm iron) feeding. Western blot images are shown in *SI Appendix*, Fig. S4C. Values, mean ± SEM. **P* < 0.05; ***P* < 0.01; ****P* < 0.001; n.s., not significant by Student's *t* test in *A*–*E*, and by one-way ANOVA with the Tukey post hoc test in *F*–*H*.

significantly elevated in the serum of both male and female *Sel1L*^{AlbCre} mice compared with *WT* littermates (Fig. 5*E*). As CP is the major copper-binding protein in the serum (4), this finding was further confirmed by the elevated copper level in the serum of *Sel1L*^{AlbCre} mice compared with *WT* littermates (*SI Appendix*, Fig. S4*B*). Elevated CP protein level and activity were also seen in the circulation of *Sel1L*^{AlbCre} mice under both HID and IDD (Fig. 5 *F* and *G* and *SI Appendix*, Fig. S4*C*). In direct contrast, TF, another hepatocyte-derived iron factor, was unaffected by the loss of ERAD under both basal and IDD conditions (Fig. 5*H* and *SI Appendix*, Fig. S4*C*), again demonstrating a CP-specific effect of SEL1L-HRD1 ERAD. Taken together, we conclude that SEL1L-HRD1 ERAD plays a key role in systemic iron distribution by regulating the abundance of CP in the system. In the absence of SEL1L-HRD1 ERAD, functional CP in the system is elevated as a result of augmented (re)folding processes in hepatocytes.

CP Links SEL1L-HRD1 ERAD to Systemic Iron Metabolism. We then asked whether CP is responsible for the altered iron homeostasis in *Sel1L*^{AlbCre} mice by knocking down CP in the liver using an i.v. injection of adeno-associated virus serotype 8 (AAV8) expressing shRNA against *Cp* (sh-*Cp*) or scramble control (sh-*scramble*). Six weeks after the AAV8 injection, sh-*Cp* efficiently reduced CP protein levels by 80 to 90% in the liver (Fig. 6 *A* and *B*) and CP activity in the circulation by 40 to 60% in both *WT* and *Sel1L*^{AlbCre} mice (Fig. 6*C*). Hepatic iron content was elevated in *WT* and *Sel1L*^{AlbCre} mice receiving AAV8-sh-*Cp* compared with those receiving sh-*scramble* (Fig. 6*D*). Iron content in the spleen of *Sel1L*^{AlbCre} mice increased upon CP knock-down, reaching a level comparable to that of *WT* mice (Fig. 6*E*). Taken together, our data demonstrate that CP links hepatic SEL1L-HRD1 ERAD to systemic iron homeostasis.

CP Disease Mutants Are SEL1L-HRD1 ERAD Substrates. Loss-of-function of CP in humans leads to an autosomal-recessive congenital disorder aceruloplasminemia, where Fe^{2+} cannot be oxidized and loaded onto TF in the circulation (46). This defect leads to pathological deposits of iron in cells such as pancreatic endocrine cells, hepatocytes, and neurons, while depriving others such as erythropoietic cells of normal iron partitioning, causing anemia, tissue iron overload, and progressive retinal and neurological degeneration (46, 47). Over 50 CP mutations have been found in humans, a few of which may be secretion incompetent and retained in the ER, leading to aceruloplasminemia (46–48). To investigate the pathological importance of SEL1L-HRD1 ERAD, we next explored its role in the pathogenicity of CP mutants.

CP is comprised of six cupredoxin-type domains (1 to 6) arranged in a triangular array (Fig. 7 *A* and *B*). Each domain, with the exception of the sixth domain, has one disulfide bond (red lines, Fig. 7 *A* and *B*) (49). We chose three ER-retained CP missense mutations, G176R, G606E, and G873E, which are located in different domains of CP for further analyses (Fig. 7 *A* and *B*) (48). We first examined how each mutation may alter protein conformation by performing 3-ms Gaussian-accelerated molecular dynamics (GaMD) simulations (50) on the WT and three mutant CP. In WT CP, G176 formed hydrogen bonds with Y160 to stabilize the interaction between two beta strands (*SI Appendix*, Fig. S5*A*). However, in the simulation of G176R mutant, new electrostatic interactions between G176R and F73 and between G176R and I175 formed, while the G176R-Y160 interaction held (*SI Appendix*, Fig. S5*B*). These extensive polar interactions formed by G176R hinder the motions of nearby residues, which reduces the flexibility of the local structure. Similar results were found in the G606E mutant. New polar interactions were introduced between G606E and Y401 and between G606E and K403 (*SI Appendix*, Fig. S5 *C* and *D*), which resulted in the shifted position of a nearby loop from P368 to G399 (*SI Appendix*, Fig. S5*E*). Although the G873E mutation did not create new polar interactions, the G873E side chain caused an increased distance between G873 and I788 from 6.90 Å to 8.18 Å, thus disturbing the stability of local structure (*SI Appendix*, Fig. S5 *F*–*H*). Hence, all three mutations potentially affect the folding of CP.

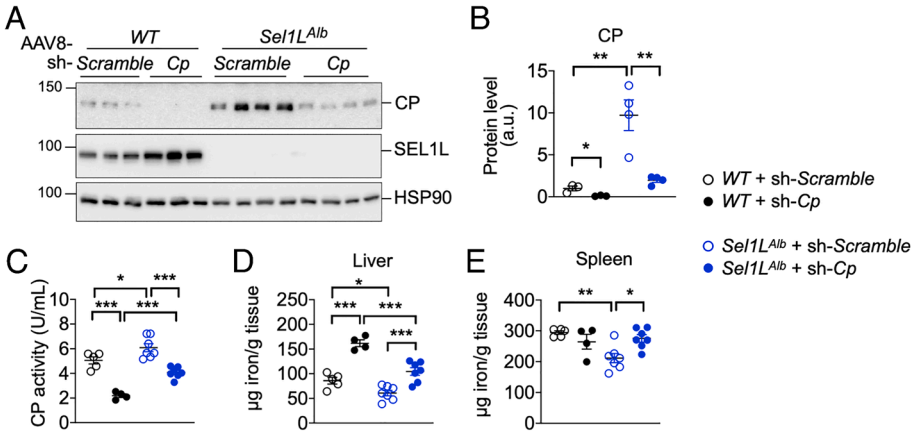

Fig. 6. SEL1L-HRD1 ERAD regulates systemic iron metabolism via CP. 7-wk-old *WT* and *Sel1L*^{AlbCre} female littermates were injected intravenously with AAV8 expressing shRNA against *Cp* or control scramble at a dose of 1 × 10^{12} viral genome copies per mouse. Six week after injection, the liver CP protein (*A* and *B*), serum CP activity (*C*), and hepatic and splenic iron levels (*D* and *E*) were examined. The quantitation of CP normalized to HSP90 is shown in (*B*). N = 4 to 7 for CP activity and tissue iron analyses. Values, mean ± SEM. **P* < 0.05; ***P* < 0.01; ****P* < 0.001 by one-way ANOVA with the Tukey post hoc test.

Next, we quantitatively assessed the impact of each mutation on protein folding efficacy (i.e., the free energy change ΔΔG) using EvoEF2 analysis (51), a newly developed empirical force field for protein design and mutation effect analysis. Interestingly, ΔΔG of the CP mutants ranged from +77.4 kcal/mol (G176R) to +217.4 kcal/mol (G606E), compared with 0 kcal/mol WT CP (Fig. 7*C*). A higher ΔΔG indicates less stability, suggesting that these missense CP mutations are conformationally unstable and prone to misfolding. Indeed, all three CP mutants were degraded by SEL1L-HRD1 ERAD, as their degradation was attenuated or abolished in *HRD1*$^{-/-}$ and *SEL1L*$^{-/-}$ HEK293T cells compared with that in *WT* cells (Fig. 7*D* and *SI Appendix*, Fig. S6*A*). Intriguingly, in this overexpression system, the half-lives of CP mutants were comparable to WT CP (*SI Appendix*, Fig. S6*A*), a likely artifact resulted from overexpression. All three mutants were ubiquitinated in a SEL1L- and HRD1-dependent manner

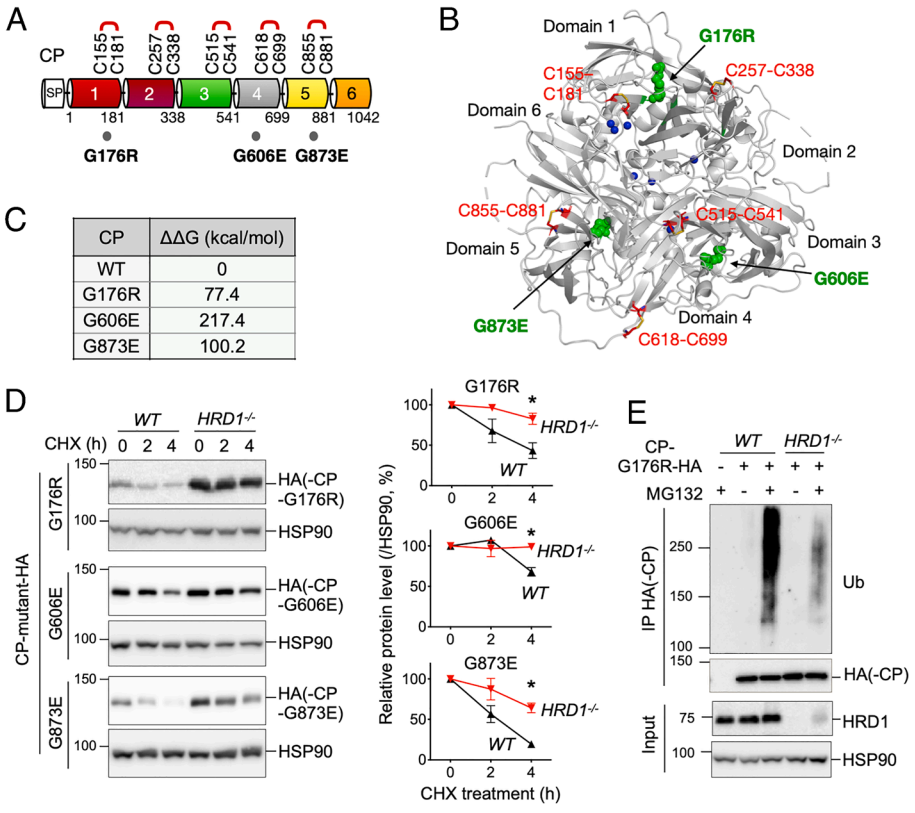

Fig. 7. CP mutants found in human aceruloplasminemia disease are degraded by SEL1L-HRD1 ERAD. (*A* and *B*) The overall structure and domain organization of human CP showing six domains, five highly conserved disulfide bonds and three missense mutations found in aceruloplasminemia patients. In (*A*), SP, signal peptide. In (*B*), the mutation sites and copper are indicated by green and blue spheres, respectively. (*C*) Predicted free energy change for different mutations using EvoEF algorithm. Lower ΔΔG means higher stability. (*D*) Western blot analysis of CP protein decay in CHX-treated *WT* and *HRD1*$^{-/-}$ HEK293T cells transfected with plasmids expressing HA-tagged CP variants. The degradation of CP quantitated relative to the percentage of control is shown on the right. Values, mean ± SEM. **P* < 0.05 by two-way ANOVA with the Tukey multiple comparison test. (*E*) Western blot analysis of immunoprecipitates of HA-agarose in *WT* and *HRD1*$^{-/-}$ HEK293T cells transfected with indicated plasmids, showing that HRD1 is required for the ubiquitination of CP with G176R mutation. Cells were treated with proteasome inhibitor MG132 or vehicle for the last 3 h prior to immunoprecipitation. (*D* and *E*) Representative data from two independent experiments are shown.

(Fig. 7*E* and *SI Appendix*, Fig. S6 *B* and *C*). Hence, these CP human variants are bona fide SEL1L-HRD1 ERAD substrates.

SEL1L-HRD1 ERAD Prevents Pathogenic Aggregation of CP Disease Mutants. Lastly, we investigated the significance of SEL1L-HRD1 ERAD in the pathogenicity of mutant CP. We examined the configuration of the mutants by separating the mutant-containing protein complexes on a nonreducing SDS-PAGE. WT CP formed largely monomers in transfected *WT*, *HRD1*$^{-/-}$ and *SEL1L*$^{-/-}$ HEK293T cells (lanes 1 and 2 in Fig. 8*A*, and lanes 2 and 3 in *SI Appendix*, Fig. S6*D*). However, three CP mutants formed significantly more high molecular weight (HMW) aggregates in *HRD1*$^{-/-}$ and *SEL1L*$^{-/-}$ cells compared with those in *WT* cells (lanes 4, 6, 8 vs. 3, 5, 7 in Fig. 8*A*, and lanes 5, 7, 9 vs. 4, 6, 8 in *SI Appendix*, Fig. S6*D*). The HMW complexes were sensitive to the treatment with a reducing agent β-mercaptoethanol (Fig. 8*A* and *SI Appendix*, Fig. S6*D*), suggesting that CP mutants form HMW aggregates via covalent disulfide bonds. Similar observations were made using sucrose gradient fractionation, where CP-G176R formed significantly more HMW aggregates in *HRD1*$^{-/-}$ cells compared with that in *WT* cells (Fig. 8*B* and quantitated in Fig. 8*C*). Taken together, we conclude that SEL1L-HRD1 ERAD attenuates pathogenic aggregation of CP mutants by targeting them for proteasomal degradation.

Discussion

In this study, we reported that the SEL1L-HRD1 ERAD complex regulates systemic iron homeostasis by regulating the maturation and turnover of CP in the ER of hepatocytes. We discovered that SEL1L-HRD1 ERAD degrades endogenous CP protein, thereby regulating its abundance in the liver and circulation. In the absence of SEL1L-HRD1 ERAD, immature CP accumulates in the ER where it undergoes (re)folding, leading to elevated secretion into circulation. This quantity control of CP is an important part of the homeostatic regulation of iron metabolism and homeostasis by enhancing iron efflux from hepatocytes. We further demonstrated that SEL1L-HRD1 ERAD also degrades disease-causing mutants of CP and thus attenuates their pathogenicity. Together, this study points to a previously unappreciated role of hepatic SEL1L-HRD1 ERAD in iron homeostasis (Fig. 8*D*).

In an unbiased proteomic analysis, over 100 proteins were significantly enriched in the purified microsomal/ER fractions from *Sel1L*-deficient livers (40), including CP, TF, ER chaperones, histocompatibility proteins, complement factors, and other secretory proteins (Fig. 3*F* and Dataset S1) (40). Further analyses demonstrated elevated quantity and secretion of CP, which contributed to the reduced hepatic and splenic iron in *Sel1L*^{AlbCre} mice (Fig. 6). This effect was CP-specific, as the total protein level and secretion of TF, as well as other iron-regulating proteins, were not altered in *Sel1L*^{AlbCre} mice (Figs. 3 *I–K* and 5*H* and *SI Appendix*, Figs. S3*G* and S4*C*). Providing further support for a CP-specific effect of SEL1L-HRD1 ERAD, many clinical cases and mouse models have shown that the loss-of-function of other key proteins in iron metabolism such as FPN1, hepcidin, TF, TFR2, and HFE as well as the gain-of-function of FPN1 lead to systemic iron overload and hemochromatosis (52–54), in direct contrast to what we reported here for *Sel1L*^{AlbCre} mice. Moreover, the ectopic expression

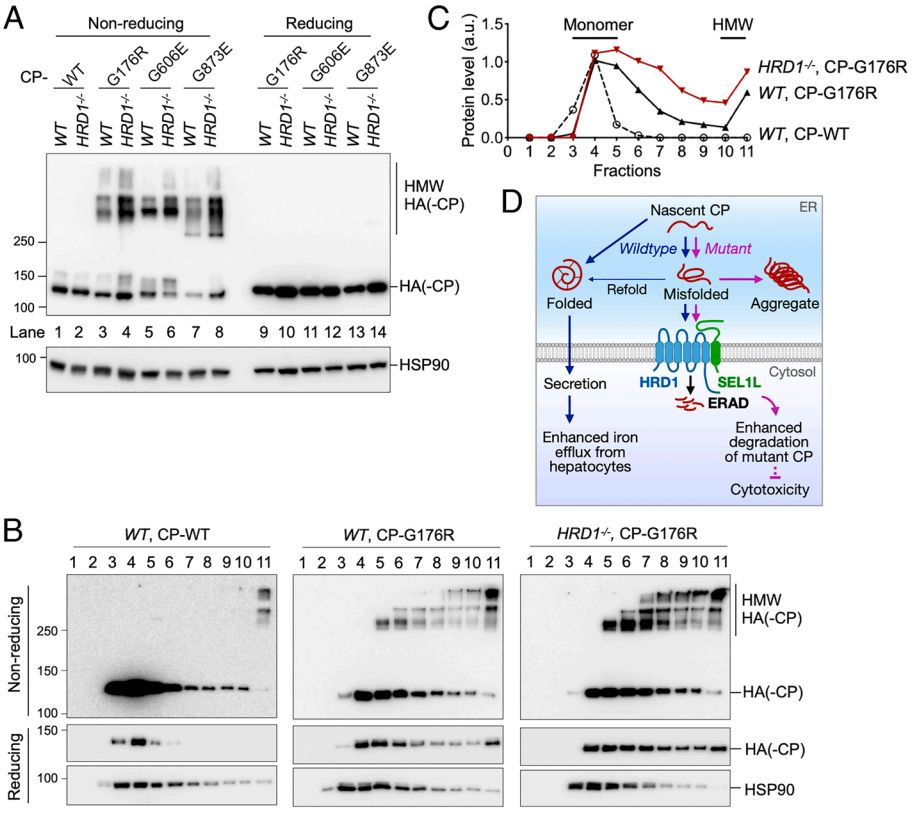

Fig. 8. SEL1L-HRD1 ERAD of CP mutants prevents their pathological aggregation. (*A*) SDS-PAGE and western blot analysis of nonreduced or reduced protein samples from *WT* and *HRD1*$^{-/-}$ HEK293T cells transfected with plasmids expressing HA-tagged CP variants as indicated. (*B* and *C*) Sucrose gradient fractionation (fractions 1 to 11 from top to bottom) of *WT* and *HRD1*$^{-/-}$ HEK293T cells transfected with a CP-WT-HA or CP-G176R-HA-expressing plasmids. Samples were analyzed by nonreducing or reducing SDS-PAGE. Quantitation of reduced CP is shown in (*C*) with fractions with CP monomers and high molecular weight (HMW) aggregates labeled. HSP90, a loading control. (*A–C*) Representative data from two independent experiments are shown. (*D*) Model showing that SEL1L-HRD1 ERAD in hepatocytes controls systemic iron homeostasis by regulating the turnover of both WT and disease mutant CP proteins under physiological and pathological conditions, respectively.

of CREBH or FGF21 in the liver led to the elevated hepatic iron content (Fig. 3 *A* and *B*) (37), while the pharmacologically induction of ER stress or disruption of UPR sensor IRE1α did not significantly alter the liver iron content (Fig. 3 *C*–*E*), further excluding major roles of CREBH, FGF21, and UPR in iron defects in *Sel1L*^{AlbCre} mice. Of note, a previous study reported that ER stress induced by tunicamycin is able to drive a trend toward elevated hepatic iron in mice (37); however, the dose used in that study was 20-fold higher than the one used in Fig. 3*C* and *SI Appendix*, Fig. S3 *C* and *D*. Further studies are required to explore whether SEL1L-HRD1 ERAD in hepatocytes regulates additional proteins in iron homeostasis.

CP is a multicopper ferroxidase known to enhance the efficiency of iron export across the plasma membrane (4). The reduced iron content in the spleen (Figs. 1*H* and 2*B* and *SI Appendix*, Fig. S2*D*) and hepatic macrophages after iron dextran injection (*SI Appendix*, Fig. S2*F*) in *Sel1L*^{AlbCre} mice suggest a gain-of-function of CP in an endocrine and paracrine manner, respectively. The elevated export of iron from the liver and spleen in *Sel1L*^{AlbCre} mice is potentially relocated to other tissues such as the heart (Fig. 1 *E* and *H* and *SI Appendix*, Fig. S2*D*). Although unclear, the specific effect in the heart may be linked to the cardiac-specific regulation of iron homeostasis via cardiomyocyte-autonomous hepcidin signaling (55). Moreover, there are two isoforms of CP generated by alternative splicing (56). The soluble isoform of CP is primarily synthesized by hepatocytes and secreted into blood plasma, while a membrane-bound glycosylphosphatidylinositol (GPI)-anchored isoform is reported in the central nervous system, testis, retina, as well as in cultured macrophages and hepatocytes (57–61). In our study, we found that the GPI-anchored CP isoform was not expressed in the mouse liver, kidney, or spleen (*SI Appendix*, Fig. S4*A*). It remains unclear whether SEL1L-HRD1 ERAD may regulate the biogenesis of GPI-anchored CP in other cell types. In addition, hephaestin is a membrane-bound homolog of CP that functions as a ferroxidase for iron absorption in the intestinal enterocytes (62–64). Given the high similarity between CP and hephaestin (50% identity) (62), it will be intriguing to examine whether enteric ERAD regulates hephaestin and thus iron absorption. In addition to a key role in iron metabolism, CP is also a major copper transporter in the plasma (65). It is estimated that 95% of copper is carried by CP in the blood (66). However, CP does not play an essential role in copper metabolism as evidenced by a normal copper homeostasis in patients with aceruloplasminemia and *Cp*$^{-/-}$ mice (67, 68). In *Sel1L*^{AlbCre}mice, the loss of SEL1L did not affect hepatic copper content, but led to an increased copper concentration in the blood (*SI Appendix*, Figs. S1*G* and S4*B*), consistent with the elevated CP secretion and activity in the circulation. It remains unclear whether elevated copper in the circulation affects iron metabolism independently of CP. During pathogen infection and inflammation, iron availability is tightly controlled and CP is induced as an acute phase protein for its antioxidant activities (46, 69). The role of ERAD in iron homeostasis under various pathological conditions remains an open question.

In the absence of SEL1L-HRD1 ERAD, the protein level and secretion of enzymatically active CP was constantly elevated independent of dietary conditions (Figs. 3 and 5 and *SI Appendix*, Fig. S3 *H* and *I*). The degradation of CP by SEL1L-HRD1 ERAD was indeed constitutive, independent of cellular iron content (*SI Appendix*, Fig. S3*J*), pointing to the importance of ERAD in controlling the abundance and activity of CP. On the other hand, SEL1L-HRD1 ERAD clears misfolded disease-causing mutants of CP and prevents them from forming HMW aggregation (Figs. 7 and 8 and *SI Appendix*, Fig. S6), thereby mediating their quality control. These results exemplify the substrate-specific effect of ERAD. Indeed, previous studies have identified a list of protein substrates either qualitatively or quantitatively regulated by SEL1L-HRD1 ERAD. For example, ERAD has been shown to control the quantity and restrain the activity of signaling proteins such as CREBH, IRE1α, transforming growth factor β receptor, nuclear factor erythroid 2-related factor 2, N6-adenosine-methyltransferase-14, and Ras homolog enriched in brain in different cell types (21, 23, 25, 27–30). WT CP is a secreted endogenous protein substrate found to be quantitatively regulated by SEL1L-HRD1 ERAD. Meanwhile, a number of misfolding-prone proteins, such as nephrin, pro-arginine-vasopressin, pro-opiomelanocortin, thrombopoietin receptor, as well as mutant CP, are cleared by SEL1L-HRD1 ERAD for quality control (20, 24, 31, 32). As suggested by our data on both WT and mutant CP, the intrinsic features of a protein to fold, misfold, and aggregate may have a significant impact on the outcome of ERAD-mediated quality and quantity control. We speculate that SEL1L-HRD1 ERAD may regulate additional proteins associated with protein-misfolding disease pathogenicity. Future therapeutic efforts may be developed to target these early folding and degradation events in the ER.

Materials and Methods

Mouse Studies. Hepatocyte-specific *Sel1L*-deficient (*Sel1L*$^{flox/flox}$;*Albumin-Cre*, i.e., *Sel1L*^{AlbCre}) mice and WT (*Sel1L*$^{flox/flox}$, *WT*) littermates, hepatocyte-specific *Hrd1*-deficient (*Hrd1*$^{flox/flox}$;*Albumin-Cre*, i.e., *Hrd1*^{AlbCre}) mice and WT (*Hrd1*$^{flox/flox}$, *WT*) littermates, *Ire1α*$^{flox/flox}$ mice, as well as hepatocyte-specific ApoE promoter-driven FGF21 transgenic or *WT* littermates were maintained on a C57BL/6J background and described previously (27, 28, 70, 71). Adenovirus-mediated overexpression of CREBH or green fluorescent protein (GFP) was performed via an intravenous injection of recombinant adenovirus as previously described (72). For baseline studies, mice were fed a standard rodent chow diet (PicoLab 5L0D, with 240 ppm iron). To induce iron deficiency or iron overload, mice were fed with an iron-deficient (Dyets D115072, with <5 ppm iron), high-iron (Dyets D115858 with 800 ppm iron, or Dyets D115854 with 8,800 ppm iron), or control diet (Dyets D110700, with 35 ppm iron) for up to 4 or 8 wk, respectively. For iron-dextran treatment, 8-wk-old mice were injected intraperitoneally with a single dose of iron-dextran (Sigma D8517) at 20 mg/kg body weight and were examined 3 d later. For CPA and tunicamycin treatment, 8-wk-old mice were injected intraperitoneally with a single dose of CPA (Sigma 239805) at 10 mg/kg body weight, tunicamycin (Tocris 3516) at 0.1 mg/kg body weight, or vehicle and were examined 4 h later. Mice were housed in a temperature-controlled environment with 12-h light/dark cycles with free access to food and water. Decapitation was used to kill the mice and tissues were immediately either fixed in 10% neutral buffered formalin or frozen in liquid nitrogen upon collection. Duodenum epithelium was collected by scraping the luminal surface of the duodenum as reported before (73).

AAV-Mediated Gene Delivery. To induce an acute deletion of IRE1α in the liver, *Ire1α*$^{f/f}$ mice were intravenously injected with AAV8-expressing hepatocyte-specific TBG promoter-driven Cre or GFP at a dose of 1.4×10^{12} viral genome copies per mouse and killed 3 wk later. To knockdown *Cp*, *WT* and *Sel1L*^{AlbCre} littermates were intravenously injected with AAV8-expressing shRNA against *Cp* or control scramble at a dose of 1×10^{12} viral genome copies per mouse and killed 6 wk later. Hairpin shRNA sequences against mouse *Cp* (CTAGCCAGTTTACTGACAGCTCATTCTCGAGAATGAGCTGTCAGTAAACTGGTTTTT) and scramble control (CTAGCGCGATAGCGCTAATAATTTCTCGAGAAATTATTAGCG CTATCGCGCTTTTT) were cloned into pCWB-U6-shRNA-CAG-eGFP vector via XbaI and SalI restriction sites. AAV8 was generated from these plasmids at the University of Michigan Vector Core (Ann Arbor, MI) on a fee-for-service basis.

Hematological, Iron/Copper Analyses, Hepcidin ELISA and CP Activity Measurement. Blood was collected by submandibular bleeding and analyzed for CBC using Heska HT5 Element analyzer at the University of Michigan In-Vivo Animal Core (Ann Arbor, MI) on a fee-for-service basis. Tissue non-heme iron contents were measured as previously reported (74). Briefly, tissues were

homogenized in a buffer containing 1 M HCl and 10% (wt/vol) trichloroacetic acid and heated for 1 h at 95 °C. Following a high-speed spin, iron was quantitated using a ferrozine solution and compared with a standard. Serum iron, ferritin, and hepcidin concentrations were measured using the Serum Iron Assay Kit (Abcam ab239715), Mouse Ferritin ELISA Kit (Abclonal RK02793), and Hepcidin Murine-Compet ELISA Kit (Intrinsic Lifesciences HMC-001), respectively, according to the manufacturer's instructions. Copper content in tissues and serum was measured using a Copper Assay Kit (Sigma MAK127) according to the manufacturer's instructions. Serum CP activity was measured using a Ceruloplasmin Colorimetric Activity Kit (Arbor Assay K035-H1) according to the manufacturer's instructions.

Isolation of Primary Hepatocytes. Mice were anesthetized with isoflurane inhalation, and the liver was perfused first with a warm perfusion buffer (Invitrogen 17701), and then with warm HBSS (Gibco 14025-076) containing 10 mM HEPES, 4 mM NaOH, and 1 mg/mL collagenase (Worthington LS004196). Digested livers were carefully removed, dispersed in a cold wash medium [Dulbecco's Modified Eagle Medium (DMEM) with 1% sodium pyruvate, 1% penicillin–streptomycin, 10% fetal bovine serum (FBS)], and passed through a 100-μm cell strainer. The cells were then washed three times by centrifugation at 50 g for 5 min at 4 °C. The resulting hepatocyte pellets were resuspended in a hepatocyte culture medium (DMEM with 1% penicillin–streptomycin and 10% FBS) and seeded in collagen-coated plates. Four hours after plating, cells were carefully washed with 1× phosphate buffered saline and cultured in a fresh hepatocyte culture medium overnight. To examine the degradation of endogenous CP, cells were pretreated with 1 μg/mL brefeldin A (BFA, Cayman Chemical 11861) for 30 min, then treated with vehicle or 150 μM cycloheximide (CHX, Sigma 01810) for 2 or 4 h. To induce iron overload or depletion, cells were treated with 100 μM FAC (MP Biomedicals 1185-57-5) or 100 μM DFO (Fisher 50-187-4275) for 21 h before the BFA and CHX treatment.

Cell Culture. *HRD1*$^{-/-}$ and *SEL1L*$^{-/-}$ HEK293T cells were generated as described previously (20, 29). HEK293T cells were cultured in DMEM (Gibco) containing 10% FBS and 1% penicillin–streptomycin and were transfected with various plasmids using 80 μg/mL polyethylenimine (PEI, Sigma 408727). After transfection, cells were treated with 10 μM MG132 (Cayman Chemical 10012628) for 3 h, or 1 μg/mL BFA (Cayman Chemical 11861) for 30 min followed by 150 μM CHX (Sigma 01810) for 2 or 4 h before collection as indicated in the figure legends. Plasmids used for transfection are: pcDNA3-mCp-Flag, pcDNA3-mCp-HA, pcDNA3-Hrd1-WT-Myc, pcDNA3-Hrd1-C2A-Myc, and pcDNA3-6His-Ub. CP point mutations (G176R, G606E, G873E) were generated using site-directed mutagenesis from pcDNA3-mCp-HA.

ER Fractionation for Western Blot Analysis. ER fractionation was performed as previously described (29). Briefly, liver samples were homogenized in a dounce grinder with buffer H (20 mM HEPES pH 7.4, 300 mM sucrose, protease inhibitor, and phosphatase inhibitor) and centrifuged at 14,000 g for 10 min. The same volume of supernatant ("Total lysate") with a normalized protein concentration was then centrifuged at 45,000 rpm at 4 °C for 1 h using a SW50.1 Swinging-Bucket Rotor (Beckman Ultracentrifuge L8M). The resulting supernatant was collected as "Non-ER" fraction. The pellet was disrupted in 200 μL 1% NP40 lysis buffer (150 mM NaCl, 1 mM EDTA, 50 mM Tris-HCl pH 7.5, 1% NP-40, protease inhibitor and phosphatase inhibitor) and collected as the "ER fraction". The same amount of the total lysate, ER, and non-ER fractions was loaded onto SDS-PAGE for western blot analysis.

Sucrose Gradient Fractionation. Sucrose gradient fractionation was performed as reported previously (29). Briefly, transfected HEK293T cells were lysed by a dounce homogenizer in 1% NP40 lysis buffer (150 mM NaCl, 1 mM EDTA, 50 mM Tris-HCl pH 7.5, 1% NP-40, protease inhibitors and 20 mM N-ethylmaleimide). Extracts were centrifuged through 20 to 40% sucrose gradients (in 150 mM NaCl, 1 mM EDTA, 50 mM Tris-HCl pH 7.5 and protease inhibitor) prepared freshly by progressively layering higher to lower density sucrose fractions in 5% increments. Extracts were centrifuged at 45,000 rpm for 17 h at 4 °C using a SW50.1 Swinging-Bucket Rotor (Beckman Ultracentrifuge L8M). Each 3.5 mL gradient was divided evenly into fractions 1 to 10 from top to bottom (330 μL each) and the pellet was resuspended in 330 μL 1% NP40 lysis buffer as fraction 11. Aliquots of fractions 1 to 11 were subjected to western blot analyses under reducing or nonreducing conditions as described below.

Immunoprecipitation. To perform immunoprecipitation for protein interactions, cells or tissue were lysed by sonication in the 1% NP40 lysis buffer (150 mM NaCl, 1 mM EDTA, 50 mM Tris-HCl pH 7.5, 1% NP-40, protease inhibitors and 5 mM N-ethylmaleimide). To analyze the ubiquitination of CP, cells were lysed in a reducing lysis buffer (150 mM NaCl, 1 mM EDTA, 50 mM Tris-HCl pH 7.5, 1% NP-40, 1% SDS, 5 mM DTT, and protease inhibitors), denatured at 95 °C for 5 min and diluted 10-fold with 1% NP40 lysis buffer before immunoprecipitation. To immunoprecipitate Flag- or HA-tagged proteins, a total of 2 to 4-mg protein lysate was precleared with protein A agarose at 4 °C for 1 h, then incubated with anti-Flag M2 agarose (Sigma A2220) or anti-HA agarose (Sigma A2095) at 4 °C overnight with gentle rocking. To immunoprecipitate BiP, a total of 2-mg tissue lysate was precleared with protein A agarose at 4 °C for 1 h, then incubated with 2 μg anti-KDEL antibody (Novus NBP1-97469) at 4 °C overnight, followed by an incubation in protein A agarose at 4 °C for 2 h. Immuno-complexes were washed in the 1% NP40 lysis buffer four times and eluted by boiling at 95 °C for 5 min in SDS sample buffer.

Endoglycosidase H (EndoH) Treatment. EndoH (New England BioLabs, P0702L) treatment was performed according to the manufacturer's protocol and as previously described (75). Briefly, tissue lysates were denatured at 95 °C for 10 min with the glycoprotein denaturing buffer, and then digested with EndoH at 37 °C for 1 h. The reaction was stopped by the addition of 5X denaturing sample buffer and boiled at 95 °C for 5 min prior to be loaded onto SDS-PAGE.

Western Blot. Preparation of cell and tissue lysates and western blotting was performed as previously described (29). For western blot of FPN1 and TFR1, lysates were not boiled before SDS-PAGE based on a previous report (76). For nonreducing SDS-PAGE, lysates were prepared in 5X nondenaturing sample buffer (250 mM Tris-HCl pH 6.8, 1% SDS, 50% glycerol and 0.05% bromophenyl blue) without boiling before being separated on an SDS-PAGE gel. The following antibodies were used in this study: CP (Abcam 48614), FTH1 (CST 4393S), TFR1 (Invitrogen 13-6800), TFR2 (Alpha Diagnostic TFR21-A), TF (Proteintech 17435-1-AP), FPN1 (Novus 21502), HFE (Abclonal A1310), ATP7B (Novus NB100-360SS), IRE1α (CST 14C10), OS9 (Abcam ab109510), Calnexin (Enzo ADI-SPA-860-D), BiP (CST C50B12), SEL1L (Abcam ab78298), HRD1 (Proteintech 13473-1-AP), CREBH (Kerafast EWS101), Ubiquitin (CST 3933), Flag (Sigma F1804 and F7425), Myc (CST 2278 and 2276), HA (Sigma H3663 and CST 3724), and HSP90 (Santa Cruz sc7947). Secondary antibodies, goat anti-rabbit or mouse IgG HRP (Bio-rad), were used at 1:6,000 dilution. Western blot membranes were developed using the Clarity Western ECL Substrate (Bio-rad) and signal was detected with a ChemiDOC imager (Bio-rad). To visualize total protein in the SDS-PAGE gel, a TGX Stain-Free Gel (Bio-rad) was used and imaged by the ChemiDOC imager. Quantification was performed using ImageLab software (Bio-rad).

RNA Extraction, RT-PCR, and Quantitative Real-Time PCR. Liver RNA was isolated as previously described (77). Briefly, total RNA from liver tissues was extracted using RNA-Stat 60 (IsoTex Diagnostics), chloroform and precipitated by isopropanol. RNA quality was determined by measuring the OD260/280 and visualized on an agarose gel. cDNA was generated using the Superscript III reverse transcriptase (Thermofisher). RT-PCR for *Xbp1* splicing (78) and *Cp* isoforms was performed using GoTaq PCR Master Mixes (Promega). Quantitative PCR (qPCR) was performed using 2X Universal SYBR Green Fast qPCR Mix (Abclonal). *18S* was used as the reference. RT-PCR and qPCR primer sequences are listed below:

For RT-PCR:
mouse *Cp* both isoforms (TGAACACCCTGAGAAAGTAAACAA, TGCATTGTGAGGCCTTGTAG),
mouse *Cp* soluble isoform (CCTGGAACCTGGTTACTCCA, CGCCAATTTATTTCATTCAGC),
mouse *Cp* GPI-anchored isoform (CCTGGAACCTGGTTACTCCA, GGATGTTCCAGGTCATCCTGT),
mouse *Xbp1* (ACACGCTTGGGAATGGACAC, CCATGGGAAGATGTTCTGGG),
mouse *L32* (GAGCAACAAGAAAACCAAGCA, TGCACACAAGCCATCTACTCA).
For qPCR:
mouse *Cp* (TGAACACCCTGAGAAAGTAAACAA, TGCATTGTGAGGCCTTGTAG),
mouse *Hepc* (AGAAAGCAGGGCAGACATTG, TTGCAACAGATACCACACTGG),
mouse *Fth1* (CTGAATGCAATGGAGTGTGC, TCTTGCGTAAGTTGGTCACG),
mouse *Ftl1* (AATGGGGTAAAACCCAGGAG, GGCTTTCCAGGAAGTCACAG),

mouse *Tfr1* (TCCGCTCGTGGAGACTACTT, ACATAGGGCGACAGGAAGTG),
mouse *Tfr2* (GACCCTGCAGTGGGTGTACT, CGACACATACTGGGACAGGA),
mouse *Tf* (ACCATGTTGTGGTCTCACGA, ACAGAAGGTCCTTGGTGGTG),
mouse *Fpn1* (TGTGAATGTGGAGCCAGTGT, ACCGTCAAATCAAAGGACCA),
mouse *Sel1L* (TGGGTTTTCTCTCTCTCCTCTG, CCTTTGTTCCGGTTACTTCTTG),
mouse *Hrd1* (AGCTACTTCAGTGAACCCCACT, CTCCTCTACAATGCCCACTGAC),
mouse *BiP* (CAAGGATTGAAATTGAGTCCTTCTT, GGTCCATGTTCAGCTCTTCAAA),
mouse *Xbp1s* (GAGTCCGCAGCAGGTG, GTGTCAGAGTCCATGGGA),
mouse *Chop* (CCAGAAGGAAGTGCATCTTCA, ACTGCACGTGGACCAGGTT),
mouse *Fgf21* (CTGGGGGTCTACCAAGCATA, CACCCAGGATTTGAATGACC),
mouse *18S* (ACCGCAGCTAGGAATAATGGA, GCCTCAGTTCCGAAAACCA).

Histology. Tissues were fixed in 10% neutralized formalin and processed by the University of Michigan In-Vivo Animal Core (Ann Arbor, MI) on a fee-for-service basis. For Prussian Blue staining with DAB enhancement, paraffin-embedded liver sections were rehydrated and stained with an iron stain (Abcam ab150674), then incubated in 3% hydrogen peroxide diluted in methanol followed by an ImmPACT DAB Substrate (Vector laboratories). DAB-enhanced Prussian blue-stained slides were photographed using a Cytation C10 Confocal Imaging Reader (BioTek).

Structure Analysis of CP Mutants. The X-ray crystallographic structure of human CP was obtained from the Protein Data Bank (4ENZ and 2J5W) (49, 79). For molecular dynamics simulation, the AMBER 14SB force field (80) and the AMBER 18 (81) package were applied by first performing 500, 5,000, and 5,000-step energy minimizations on hydrogen atoms, side-chains, and the entire protein system, respectively, then solvating by the TIP3P water model (82). The water and the entire system were minimized for 1,000 and 5,000 steps, respectively. To equilibrate the system, a molecular dynamics (MD) simulation was performed on the water molecules for 100 ps at 300 K, then the entire system was gradually heated from 50 K to 300 K with the increment of 50 K for 10 ps on each temperature. The timestep of the MD simulations was 2 fs. After MD simulations, GaMD simulations (83) was performed with an updated boost potential for 50 ns, followed by a 3-μs production simulation with a fixed boost potential for all systems. The average and SD of the system potential energies were calculated every 500 ps. The upper limit of the SD of the potential energy was set to 6.0 kcal/mol. The GaMD trajectory every 10 ps was saved for analysis. The analysis of hydrogen bonding and atom–atom distance was computed by the VMD (84) and CPPTRJ program (85). C-I-TASSER and EvoEF2 (51, 86) were used to analyze the impact of mutations on the protein folding in terms of ΔΔG, i.e., the free energy change caused by single mutation.

Statistics. Unpaired two-tailed Student's *t* test was used for two-group analyses. Two-way ANOVA with the Tukey multiple comparison test or one-way ANOVA with the Tukey post hoc test was used for multigroup analyses (GraphPad Prism). Data were presented as the mean ± SEM; $P < 0.05$ was considered significant.

Study Approval. All animal procedures were approved by the Institutional Animal Care and Use Committee of Wayne State University.

Data, Materials, and Software Availability. All study data are included in the article and/or *SI Appendix*. Previously published data were used for this work [GSE118658 from Bhattacharya et al. (27). PXD035243 from Bhattacharya et al. (40)].

ACKNOWLEDGMENTS. We thank Drs. Yuan Zhang, David J. Mangelsdorf and Steven A. Kliewer for sharing reagents; Drs. Ling Qi, Yi Xiong and members of the Sun laboratories for their technical assistance and insightful discussions. We also thank the Wayne State University Microscopy, Imaging and Cytometry Resources Core, Michigan Diabetes Research Center, University of Michigan In-vivo Animal Core, and Vector Core for their support. This work was supported by the NIH (R01DK128077 to S.S.; R01CA148828, R01CA245546, and R01DK095201 to Y.M.S.; R01DK126908 to K.Z.; R01DK120330, and R01DK126908 to D.F.), Wayne State University Research Grant (to S.S.), Wayne State University Startup Grant (to Y.M.H.), and the Richard Barber Interdisciplinary Research Program (to S.S., Y.M.H., and M.S.).

Author affiliations: [a]Center for Molecular Medicine and Genetics, Wayne State University School of Medicine, Detroit, MI 48201; [b]Department of Molecular & Integrative Physiology, University of Michigan Medical School, Ann Arbor, MI 48105; [c]Department of Physics and Astronomy, Wayne State University, Detroit, MI 48201; [d]Department of Pathology, Northwestern University Feinberg School of Medicine, Chicago, IL 60611; [e]Department of Biochemistry, Microbiology and Immunology, Wayne State University School of Medicine, Detroit, MI 48201; and [f]Department of Internal Medicine, University of Michigan Medical School, Ann Arbor, MI 48109

1. K. N. White *et al.*, The transfer of iron between ceruloplasmin and transferrins. *Biochim. Biophys. Acta.* **1820**, 411–416 (2012).
2. I. V. Milto, I. V. Suhodolo, V. D. Prokopieva, T. K. Klimenteva, Molecular and cellular bases of iron metabolism in humans. *Biochemistry (Mosc)* **81**, 549–564 (2016).
3. C. Y. Wang, J. L. Babitt, Liver iron sensing and body iron homeostasis. *Blood* **133**, 18–29 (2019).
4. N. E. Hellman, J. D. Gitlin, Ceruloplasmin metabolism and function. *Annu. Rev. Nutr.* **22**, 439–458 (2002).
5. S. Dev, J. L. Babitt, Overview of iron metabolism in health and disease. *Hemodial. Int.* **21 Suppl**, S6–S20 (2017).
6. R. E. Fleming, P. Ponka, Iron overload in human disease. *N. Engl. J. Med.* **366**, 348–359 (2012).
7. A. Yiannikourides, G. O. Latunde-Dada, A short review of iron metabolism and pathophysiology of iron disorders. *Medicines (Basel)* **6**, 85 (2019).
8. L. Qi, B. Tsai, P. Arvan, New insights into the physiological role of endoplasmic reticulum-associated degradation. *Trends Cell Biol.* **27**, 430–440 (2017).
9. C. J. Guerriero, J. L. Brodsky, The delicate balance between secreted protein folding and endoplasmic reticulum-associated degradation in human physiology. *Physiol. Rev.* **92**, 537–576 (2012).
10. R. Y. Hampton, R. G. Gardner, J. Rine, Role of 26S proteasome and HRD genes in the degradation of 3-hydroxy-3-methylglutaryl-CoA reductase, an integral endoplasmic reticulum membrane protein. *Mol. Biol. Cell* **7**, 2029–2044 (1996).
11. J. C. Christianson *et al.*, Defining human ERAD networks through an integrative mapping strategy. *Nat. Cell Biol.* **14**, 93–105 (2012).
12. B. Mueller, B. N. Lilley, H. L. Ploegh, SEL1L, the homologue of yeast Hrd3p, is involved in protein dislocation from the mammalian ER. *J. Cell Biol.* **175**, 261–270 (2006).
13. R. G. Gardner *et al.*, Endoplasmic reticulum degradation requires lumen to cytosol signaling. Transmembrane control of Hrd1p by Hrd3p. *J. Cell Biol.* **151**, 69–82 (2000).
14. R. K. Plemper *et al.*, Genetic interactions of Hrd3p and Der3p/Hrd1p with Sec61p suggest a retro-translocation complex mediating protein transport for ER degradation. *J. Cell Sci.* **112**, 4123–4134 (1999).
15. P. Carvalho, V. Goder, T. A. Rapoport, Distinct ubiquitin-ligase complexes define convergent pathways for the degradation of ER proteins. *Cell* **126**, 361–373 (2006).
16. B. Mueller, E. J. Klemm, E. Spooner, J. H. Claessen, H. L. Ploegh, SEL1L nucleates a protein complex required for dislocation of misfolded glycoproteins. *Proc. Natl. Acad. Sci. U.S.A.* **105**, 12325–12330 (2008).
17. M. Sundaram, I. Greenwald, Suppressors of a lin-12 hypomorph define genes that interact with both lin-12 and glp-1 in Caenorhabditis elegans. *Genetics* **135**, 765–783 (1993).
18. S. Sun *et al.*, Sel1L is indispensable for mammalian endoplasmic reticulum-associated degradation, endoplasmic reticulum homeostasis, and survival. *Proc. Natl. Acad. Sci. U.S.A.* **111**, E582–591 (2014).
19. A. Bhattacharya, L. Qi, ER-associated degradation in health and disease-from substrate to organism. *J. Cell Sci.* **132**, jcs232850 (2019).
20. S. Yoshida *et al.*, Endoplasmic reticulum-associated degradation is required for nephrin maturation and kidney glomerular filtration function. *J. Clin. Invest.* **131**, e143988 (2021).
21. N. Shrestha *et al.*, Sel1L-Hrd1 ER-associated degradation maintains beta cell identity via TGF-beta signaling. *J. Clin. Invest.* **130**, 3499–3510 (2020).
22. Z. Zhou *et al.*, Endoplasmic reticulum-associated degradation regulates mitochondrial dynamics in brown adipocytes. *Science* **368**, 54–60 (2020).
23. L. Liu *et al.*, ER-associated degradation preserves hematopoietic stem cell quiescence and self-renewal by restricting mTOR activity. *Blood* **136**, 2975–2986 (2020).
24. L. Xu *et al.*, Protein quality control through endoplasmic reticulum-associated degradation maintains haematopoietic stem cell identity and niche interactions. *Nat. Cell Biol.* **22**, 1162–1169 (2020).
25. J. Wei *et al.*, HRD1-mediated METTL14 degradation regulates m(6)A mRNA modification to suppress ER proteotoxic liver disease. *Mol. Cell* **81**, 5052–5065.e5056 (2021).
26. H. Kim *et al.*, Regulation of hepatic circadian metabolism by the E3 ubiquitin ligase HRD1-controlled CREBH/PPARalpha transcriptional program. *Mol. Metab.* **49**, 101192 (2021).
27. A. Bhattacharya *et al.*, Hepatic Sel1L-Hrd1 ER-associated degradation (ERAD) manages FGF21 levels and systemic metabolism via CREBH. *EMBO J.* **37**, e99277 (2018).
28. J. Wei *et al.*, HRD1-ERAD controls production of the hepatokine FGF21 through CREBH polyubiquitination. *EMBO J.* **37**, e98942 (2018).
29. S. Sun *et al.*, IRE1alpha is an endogenous substrate of endoplasmic-reticulum-associated degradation. *Nat. Cell Biol.* **17**, 1546–1555 (2015).
30. T. Wu *et al.*, Hrd1 suppresses Nrf2-mediated cellular protection during liver cirrhosis. *Genes. Dev.* **28**, 708–722 (2014).
31. G. Shi *et al.*, ER-associated degradation is required for vasopressin prohormone processing and systemic water homeostasis. *J. Clin. Invest.* **127**, 3897–3912 (2017).
32. G. H. Kim *et al.*, Hypothalamic ER-associated degradation regulates POMC maturation, feeding, and age-associated obesity. *J. Clin. Invest.* **128**, 1125–1140 (2018).
33. H. J. Sim *et al.*, Augmented ERAD (ER-associated degradation) activity in chondrocytes is necessary for cartilage development and maintenance. *Sci. Adv.* **8**, eabl4222 (2022).
34. Z. Zhang *et al.*, Ferroportin1 deficiency in mouse macrophages impairs iron homeostasis and inflammatory responses. *Blood* **118**, 1912–1922 (2011).
35. M. Musumeci *et al.*, Iron excretion in iron dextran-overloaded mice. *Blood Transfus* **12**, 485–490 (2014).
36. A. Daba, K. Gkouvatsos, G. Sebastiani, K. Pantopoulos, Differences in activation of mouse hepcidin by dietary iron and parenterally administered iron dextran: compartmentalization is critical for iron sensing. *J. Mol. Med (Berl)* **91**, 95–102 (2013).

37. C. Vecchi *et al.*, ER stress controls iron metabolism through induction of hepcidin. *Science* **325**, 877–880 (2009).
38. A. Heifetz, R. W. Keenan, A. D. Elbein, Mechanism of action of tunicamycin on the UDP-GlcNAc:dolichyl-phosphate Glc-NAc-1-phosphate transferase. *Biochemistry* **18**, 2186–2192 (1979).
39. M. Cnop *et al.*, Selective inhibition of eukaryotic translation initiation factor 2 alpha dephosphorylation potentiates fatty acid-induced endoplasmic reticulum stress and causes pancreatic beta-cell dysfunction and apoptosis. *J. Biol. Chem.* **282**, 3989–3997 (2007).
40. A. Bhattacharya *et al.*, SEL1L-HRD1 ER-associated degradation suppresses hepatocyte hyperproliferation and liver cancer. *iScience* **25**, 105183 (2022).
41. Y. Ye, S. H. Baek, Y. Ye, T. Zhang, Proteomic characterization of endogenous substrates of mammalian ubiquitin ligase Hrd1. *Cell Biosci.* **8**, 46 (2018).
42. P. Pisu, D. Bellovino, S. Gaetani, Copper regulated synthesis, secretion and degradation of ceruloplasmin in a mouse immortalized hepatocytic cell line. *Cell. Mol. Biol.* **Suppl 51**, OL859–867 (2005).
43. M. Sato, J. D. Gitlin, Mechanisms of copper incorporation during the biosynthesis of human ceruloplasmin. *J. Biol. Chem.* **266**, 5128–5134 (1991).
44. J. D. Gitlin, Wilson disease. *Gastroenterology* **125**, 1868–1877 (2003).
45. A. Harazono *et al.*, Site-specific N-glycosylation analysis of human plasma ceruloplasmin using liquid chromatography with electrospray ionization tandem mass spectrometry. *Anal. Biochem.* **348**, 259–268 (2006).
46. S. Kono, Aceruloplasminemia: An update. *Int. Rev. Neurobiol.* **110**, 125–151 (2013).
47. A. Doyle, F. Rusli, P. Bhathal, Aceruloplasminaemia: A rare but important cause of iron overload. *BMJ Case Rep.* **2015**, bcr2014207541 (2015).
48. S. Kono *et al.*, Biological effects of mutant ceruloplasmin on hepcidin-mediated internalization of ferroportin. *Biochim. Biophys. Acta* **1802**, 968–975 (2010).
49. I. Bento, C. Peixoto, V. N. Zaitsev, P. F. Lindley, Ceruloplasmin revisited: Structural and functional roles of various metal cation-binding sites. *Acta. Crystallogr. D Biol. Crystallogr.* **63**, 240–248 (2007).
50. Y. Miao, V. A. Feher, J. A. McCammon, Gaussian accelerated molecular dynamics: Unconstrained enhanced sampling and free energy calculation. *J. Chem. Theory. Comput.* **11**, 3584–3595 (2015).
51. X. Huang, R. Pearce, Y. Zhang, EvoEF2: Accurate and fast energy function for computational protein design. *Bioinformatics* **36**, 1135–1142 (2019).
52. R. E. Fleming, Q. Feng, R. S. Britton, Knockout mouse models of iron homeostasis. *Annu. Rev. Nutr.* **31**, 117–137 (2011).
53. P. Brissot *et al.*, Haemochromatosis. *Nat. Rev. Dis. Primers* **4**, 18016 (2018).
54. L. Jiang *et al.*, RNF217 regulates iron homeostasis through its E3 ubiquitin ligase activity by modulating ferroportin degradation. *Blood* **138**, 689–705 (2021).
55. S. Lakhal-Littleton *et al.*, An essential cell-autonomous role for hepcidin in cardiac iron homeostasis. *eLife* **5**, e19804 (2016).
56. F. M. Yang *et al.*, Human ceruloplasmin. Tissue-specific expression of transcripts produced by alternative splicing. *J. Biol. Chem.* **265**, 10780–10785 (1990).
57. B. N. Patel, S. David, A novel glycosylphosphatidylinositol-anchored form of ceruloplasmin is expressed by mammalian astrocytes. *J. Biol. Chem.* **272**, 20185–20190 (1997).
58. B. Mittal, M. M. Doroudchi, S. Y. Jeong, B. N. Patel, S. David, Expression of a membrane-bound form of the ferroxidase ceruloplasmin by leptomeningeal cells. *Glia* **41**, 337–346 (2003).
59. R. R. Fortna, H. A. Watson, S. E. Nyquist, Glycosyl phosphatidylinositol-anchored ceruloplasmin is expressed by rat Sertoli cells and is concentrated in detergent-insoluble membrane fractions. *Biol. Reprod* **61**, 1042–1049 (1999).
60. L. Chen *et al.*, Increased expression of ceruloplasmin in the retina following photic injury. *Mol. Vis.* **9**, 151–158 (2003).
61. L. Marques *et al.*, Immune cells and hepatocytes express glycosylphosphatidylinositol-anchored ceruloplasmin at their cell surface. *Blood Cells Mol. Dis.* **48**, 110–120 (2012).
62. C. D. Vulpe *et al.*, Hephaestin, a ceruloplasmin homologue implicated in intestinal iron transport, is defective in the sla mouse. *Nat. Genet.* **21**, 195–199 (1999).
63. D. M. Frazer *et al.*, Cloning and gastrointestinal expression of rat hephaestin: Relationship to other iron transport proteins. *Am. J. Physiol. Gastrointest Liver Physiol.* **281**, G931–G939 (2001).
64. B. K. Fuqua *et al.*, Severe iron metabolism defects in mice with double knockout of the multicopper ferroxidases hephaestin and ceruloplasmin. *Cell Mol. Gastroenterol. Hepatol.* **6**, 405–427 (2018).
65. C. Doguer, J. H. Ha, J. F. Collins, Intersection of iron and copper metabolism in the mammalian intestine and liver. *Compr. Physiol.* **8**, 1433–1461 (2018).
66. Z. L. Harris, J. D. Gitlin, Genetic and molecular basis for copper toxicity. *Am. J. Clin. Nutr.* **63**, 836S–841S (1996).
67. T. Y. Tao, J. D. Gitlin, Hepatic copper metabolism: Insights from genetic disease. *Hepatology* **37**, 1241–1247 (2003).
68. Z. L. Harris, A. P. Durley, T. K. Man, J. D. Gitlin, Targeted gene disruption reveals an essential role for ceruloplasmin in cellular iron efflux. *Proc. Natl. Acad. Sci. U.S.A.* **96**, 10812–10817 (1999).
69. U. E. Schaible, S. H. Kaufmann, Iron and microbial infection. *Nat. Rev. Microbiol.* **2**, 946–953 (2004).
70. Y. Zhang *et al.*, The starvation hormone, fibroblast growth factor-21, extends lifespan in mice. *eLife* **1**, e00065 (2012).
71. T. Iwawaki, R. Akai, S. Yamanaka, K. Kohno, Function of IRE1 alpha in the placenta is essential for placental development and embryonic viability. *Proc. Natl. Acad. Sci. U.S.A.* **106**, 16657–16662 (2009).
72. H. Kim, Z. Zheng, P. D. Walker, G. Kapatos, K. Zhang, CREBH maintains circadian glucose homeostasis by regulating hepatic glycogenolysis and gluconeogenesis. *Mol. Cell Biol.* **37**, e00048-17 (2017).
73. N. K. Das *et al.*, Microbial metabolite signaling is required for systemic iron homeostasis. *Cell Metab.* **31**, 115–130.e116 (2020).
74. C. J. Rebouche, C. L. Wilcox, J. A. Widness, Microanalysis of non-heme iron in animal tissues. *J. Biochem. Biophys. Methods* **58**, 239–251 (2004).
75. H. Sha *et al.*, The ER-associated degradation adaptor protein Sel1L regulates LPL secretion and lipid metabolism. *Cell Metab.* **20**, 458–470 (2014).
76. Y. Tsuji, Transmembrane protein western blotting: Impact of sample preparation on detection of SLC11A2 (DMT1) and SLC40A1 (ferroportin). *PLoS One* **15**, e0235563 (2020).
77. K. C. Coate *et al.*, FGF21 is an exocrine pancreas secretagogue. *Cell Metab.* **25**, 472–480 (2017).
78. S. Sun, S. Kelekar, S. A. Kliewer, D. J. Mangelsdorf, The orphan nuclear receptor SHP regulates ER stress response by inhibiting XBP1s degradation. *Genes. Dev.* **33**, 1083–1094 (2019).
79. V. R. Samygina *et al.*, Ceruloplasmin: Macromolecular assemblies with iron-containing acute phase proteins. *PLoS One* **8**, e67145 (2013).
80. V. Hornak *et al.*, Comparison of multiple amber force fields and development of improved protein backbone parameters. *Proteins Struct. Funct. Bioinf.* **65**, 712–725 (2006).
81. D. A. Case *et al.*, AMBER (University of California, San Francisco, 2015).
82. S. Izadi, A. V. Onufriev, Accuracy limit of rigid 3-point water models. *J. Chem. Phys.* **145**, 074501 (2016).
83. Y. Miao, V. A. Feher, J. A. McCammon, Gaussian accelerated molecular dynamics: Unconstrained enhanced sampling and free energy calculation. *J. Chem. Theory. Comput.* **11**, 3584–3595 (2015).
84. W. Humphrey, A. Dalke, K. Schulten, VMD: Visual molecular dynamics. *J. Mol. Graphics* **14**, 33–38 (1996).
85. D. R. Roe, T. E. Cheatham, PTRAJ and CPPTRAJ: Software for processing and analysis of molecular dynamics trajectory data. *J. Chem. Theory. Comput.* **9**, 3084–3095 (2013).
86. W. Zheng *et al.*, Deep-learning contact-map guided protein structure prediction in CASP13. *Proteins* **87**, 1149–1164 (2019).